Proceedings of the ASME 2010 3rd Joint US-European Fluids Engineering Summer Meeting and 8th International Conference on Nanochannels, Microchannels, and Minichannels
FEDSM-ICNMM2010
August 1-5, 2010, Montreal, Canada

FEDSM-ICNMM2010-31248

LIQUID JET IMPINGEMENT ON A FREE LIQUID SURFACE: PIV STUDY OF THE TURBULENT BUBBLY TWO-PHASE FLOW

Khaled J. Hammad
Dantec Dynamics, Inc.
Ramsey, NJ, USA

ABSTRACT

The turbulent two-phase flow arising from the normal impingement of a round free-surface water jet on a horizontal air-water interface was experimentally studied. Due to the weakly viscous nature of the flow system under consideration, external perturbations or small variations in jet inflow conditions can lead to drastically different flow field characteristics under seemingly similar test conditions. In the current study, a fully developed turbulent jet, exiting a long pipe, ensured properly characterized inflow conditions. The study considered two jet inflow conditions; one entrained air and created a bubbly two-phase flow field while the other did not. Particle image velocimetry (PIV) was used to characterize the flow field beneath the interface, with and without air entrainment, for various nozzle-to-interface separation distances. Turbulent velocity fields of the continuous-phase and dispersed-phase were simultaneously measured in the developing flow region and presented using Reynolds decomposition into mean and fluctuating components. The mean and RMS velocities of the two-phase flow field were compared with velocity measurements obtained under single-phase conditions.

NOMENCLATURE

d	Nozzle internal diameter (m)
H	Nozzle-to-interface separation distance (m)
L	Pipe length (m)
Re	Reynolds number ($U_b d/\nu$)
U	Mean velocity magnitude (m/s)
U_b	Jet bulk velocity at nozzle exit (m/s)
U_{ci}	Mean centerline velocity at interface
U_c	Mean centerline velocity at the nozzle exit (m/s)
r, z	Cylindrical coordinates (m)
u_r, u_z	Instantaneous velocity in z and r directions (m/s)
u	Normalized mean velocity $\overline{u_z}/u_c$ in z direction
v	Normalized mean velocity $\overline{u_r}/u_c$ in r direction
u_r', u_z'	Velocity fluctuations in r and z directions (m/s)
$\overline{u_r'^2}, \overline{u_z'^2}$	Normal Reynolds stresses (m^2/s^2)
$\overline{u_r' u_z'}$	Shear Reynolds stress (m^2/s^2)
u'	Normalized RMS velocity $\sqrt{\overline{u_z'^2}}/U_c$ in z direction
v'	Normalized RMS velocity $\sqrt{\overline{u_r'^2}}/U_c$ in r direction

Greek Symbols

ρ	Density
ν	Kinematic viscosity of jet fluid (m^2/s)
ω	Vorticity normalized by $2\pi U_b/d$

Subscripts

b	Bulk
c	Centerline
i	Interface
j	Jet
r	Radial
z	Vertical

INTRODUCTION

The interaction of liquid jets with free surfaces can be encountered in nature, *e.g.* waterfalls and waves in ocean [1], and in industrial applications. Air entrainment and subsurface bubbly flow were found to take place once the jet velocity impacting the free surface exceeded a critical value [2]. The direct impingement of a free liquid jet on a liquid surface was recognized as an efficient method for producing gas bubbles in

liquids and has been utilized in numerous industrial processes for aeration and heat/mass transfer enhancement [3-5]. Due to it's fundamental and practical importance, this problem has been extensively studied in the past [6-15]. The bulk of available research work focused on quantifying air entrainment and size distribution and penetration depth of bubbles entrained by the jet under various test conditions. The comprehensive review by Bin [8] about air entrainment by plunging jets presented a summary of the correlations established to predict the onset of air entrainment based on a critical velocity of the jet, amount of entrained air, and diameter distributions within the bubbly plum.

The reviews by Bin [8] and Chanson [10] highlighted the fact that most previous studies were qualitative and only a small number of researchers studied the flow field below impingement surface. McKeogh and Ervine [6] reported velocity distributions primarily in the fully developed flow region while Bonetto and Lahey [9] presented results obtained in both developing and fully developed flow regions. Iguchi *et. al.* [16] used LDV to study the liquid-phase motion in the bubble dispersion region when injecting water vertically downward through a straight circular pipe onto a water bath. Turbulence levels were higher than the single-phase free jet flow case, mainly due to turbulence production in the wake of bubbles. Reliable LDV measurements were not possible in the flow developing region and were restricted to >16 pipe diameters beneath the bath surface. The more recent study by Chanson *et. al.* [17] investigates air entrainment and bubble dispersion in the developing flow region of vertical circular plunging jets. Clear water jet velocities and turbulent velocity fluctuations were measured in the free-falling jet using Pitot tubes and hot-film probes while air–water flow properties were measured with single-tip conductivity probes.

Air entrainment and subsequent breakup into bubbles depends on the physical properties of the fluids used, nozzle geometry, nozzle-free surface separation, jet velocity and turbulence, and instabilities at the jet surface [6, 7, 11, 12].

The primary mechanisms leading to air entrainment are the interfacial shear along the liquid jet interface which drags down an air boundary layer and the developing interfacial perturbations which leads to air entrapment at the point of impact of the plunging jet with the free surface of the receiving pool [13]. The annular air sheet dragged down by the liquid jet beneath the free surface of the pool becomes unstable under the effect of the shear and the entrapped pockets of air break up into bubbles. The produced bubbles undergo a further break up process into smaller bubbles due to the turbulence generated by the submerged jet within the shear-layer. The study by Oguz [11] confirmed that the size of the largest bubbles produced correlates to the wavelength of the jet surface roughness resulting from boundary layer instability inside the nozzle. The maximum bubble size was nearly equal to one quarter of the wavelength of the jet surface disturbance which is consistent with a breakup process of relatively large air pockets around the jet.

The two-phase turbulent nature of the flow combined with the importance of inertia, viscous, surface tension, and gravity forces complicate the task of coming up with a single physical model that can describe and predict the evolution of the flow events. Studying and modeling the physical mechanisms at work becomes even more difficult for weakly viscous flows. Weakly viscous flow systems, like the turbulent air-water flow field under consideration here, are sensitive to ambient perturbations, such as free surface instability and external vibrations, which can significantly affect the air entrapment process and the subsequent flow evolution [14]. Previous modeling work produced semi-empirical correlations that predict parameters such as the volume of entrained air, bubble size distributions, or the depth of penetration of the bubbles. These correlations were valid only over a restrictive range of parameters.

Despite the available body of knowledge, the two-phase nature of flow remains poorly understood. More work is needed to improve our understanding of the mechanisms that play a role in the air-entrapment process at the impinging point and at the fluctuating interface of both the jet and the free surface of the receiving pool. An examination of the available literature reveals a lack of air-water flow field information near the impingement surface.

The current study investigates the turbulent two-phase flow field characteristics in the developing flow region beneath the impingement surface. A schematic of the current flow problem is shown in Fig. 1. A fully developed turbulent jet with a mean exit velocity U_b is ejected vertically downward from a pipe nozzle of diameter d, located at a distance H from a pool surface. The current work is based on well defined inflow conditions and controlled experiments that minimized the potential influence of external perturbation such as vibrations or external aerodynamic forces.

EXPERIMENTAL SETUP

The closed-loop flow system used here comprised of a water tank, pump, flowmeter, pipe, pipe mounting and positioning structure. The rectangular glass tank used was 508 mm long, 254 mm wide and 305 mm high. The tank walls were approximately 6 mm thick. The jet was produced using a vertical type 316 stainless steel precision pipe placed on the cylinder centerline with an inner diameter d = 10.92 mm, a length L = 914.4 mm and a wall thickness 0.889 mm. The length-to-diameter ratio of the pipe, L/d = 84, assured a fully developed turbulent flow conditions at the outlet. The jet was positioned 127 mm, about 12d, away from the walls of the tank. The filled height of the tank was 270 mm, 25d.

As shown in Fig. 1, the separation distance between the pipe outlet and the air/water interface is denoted by H. The origin of the cylindrical r, z coordinate system coincides with intersection point of the jet centerline and the free surface. The axial coordinate, z, is pointing downward away from the free surface while the radial one, r, is measured along the horizontal free surface.

Measurements were performed at four nozzle-to-interface separation distances, *H/d*= -1, 0, 1, 2 and 3. Two constant volumetric flow rates of 0.945 x 10^{-4} m^3/s (1.5 GPM) and 1.575 × 10^{-4} m^3/s (2.5 GPM) were used, resulting in a fixed pipe bulk velocities, U_b, of 1.01 and 1.68 m/s. The kinematic viscosity of the working fluid, water at 28°C and 30°C, were 8.38 × 10^{-7} m^2/s and 8.00 × 10^{-7} m^2/s. The corresponding Reynolds numbers, $\mathrm{Re} = U_b D/\nu$, were 22,962 and 13,153.

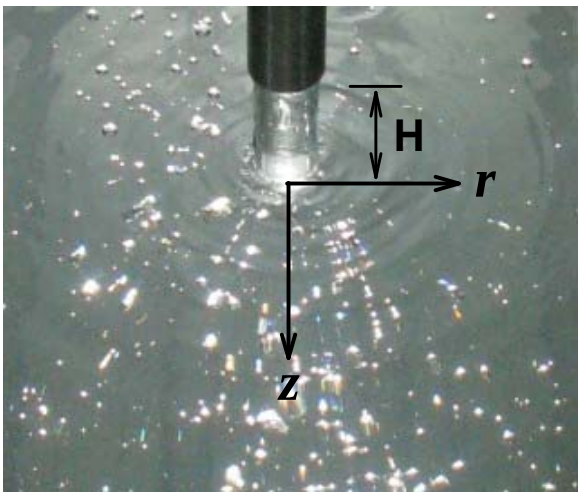

Fig.1 Free surface impinging jet and coordinate system

PIV SYSTEM

A Dantec Dynamics two-dimensional Time-Resolved PIV system was used to measure the flow field along each *r-z* plane of interest. It consisted of a diode pumped, dual cavity, Nd:YLF laser system with an output energy of 15 mJ, 527nm per cavity with a typical laser pulse duration of 150 ns @1kHz. A maximum of 10 kHz firing frequency per cavity can be achieved. Laser beam divergence was <5 mrad, beam diameter about 3 mm and pulse stability ±1%. The imaging system allowed for the capture of un-interrupted 6,000 CMOS camera images at a sampling rate of 2 kHz and a resolution of 1280 x 1024 pixels. Synchronization hardware for controlling the laser and camera and software running on a Windows-based platform for data acquisition, management and post-analysis were also used.

Light sheet forming optics mounted at the exit portal of the laser system generated a thin, focusable light sheet by means of a series of spherical and cylindrical lenses. A vertical divergent light sheet was generated and used to illuminate the full extent of the measurement region within the tank. The vertical light sheet was aligned to pass through the center of the pipe. The thickness of the light sheet at the imaging plane was 1.5 mm. The spatial location of the illumination system was fixed during all the tests. A micrometer was used to position the CMOS camera perpendicular to the laser sheet and properly align and optimize the imaged area. The imaging lens was a 60-mm *f*2.8 Nikkor. Nearly neutrally buoyant 50 μm Polymide particles having a density of 1.05 g/cm^3 were used as tracer particles for the liquid-phase. The density of the test fluid, water at about 30°C, was 0.996 g/cm^3.

DATA PROCESSING

Captured bubbly flow images, Fig. 2a, were pre-processed using a sequence of low-pass, high-pass and morphology digital filters for background subtraction, bubble detection and phase separation. The areas occupied by bubbles were identified using median filtering, Fig. 2c, and then subtracted from enhanced captured images, Fig. 2b, to produce the liquid-phase or seeding particle image, Fig. 2d.

Both the liquid and bubble flow fields were evaluated using an adaptive correlation technique. For the present set of measurements, a high-accuracy multi-pass adaptive cross-correlation technique was utilized to evaluate the velocity field determined from each pair of particle images. The signal strength was further optimized by window off-set which minimized particle drop-outs. A high sub-pixel accuracy that is independent of correlation peak shape was achieved and further minimized displacement estimate errors [18].

The final interrogation area, IA, was 64 × 64 pixels with 75% overlap in both the horizontal and vertical directions. An initial IA of 256 × 256 pixels was sequentially reduced to the final IA. A dynamic second-order accurate method was used to spatially offset the two IA's during each subsequent iteration cycle by the displacement calculated from previous steps. During each iteration cycle, checks on the correlation's signal-to-noise, as well as a local comparison of vector attributes with the median value of 5 × 5 neighbors were applied to validate and remove outliers. To remove spurious vectors, a minimum peak height ratio (between the 1st and 2nd peak) of 1.2 was selected, thereby putting more stringent conditions on peak identification for the subsequent determination of vectors.

For each test case, 2000 PIV realizations at a sampling rate of 200 Hz were obtained and used to evaluate the mean and RMS flow field information presented here. The focus of the current work was to investigate the multiphase flow structure in the vicinity of the submerged jet shear layer, the developing flow region. The results shown represent approximately a 5D x 8D area, 51 x 84 mm, situated beneath the impingement interface. Each field of view occupied 640 x 1040 Pixels and resulted in a total of 37 x 62 or 2294 vectors for each PIV data set.

NOZZLE EXIT FLOW CONDITIONS

The pipe exit region was analyzed to investigate the flow conditions 0.25*d* from the nozzle for a nozzle height *H*=0, liquid-phase flow only case.

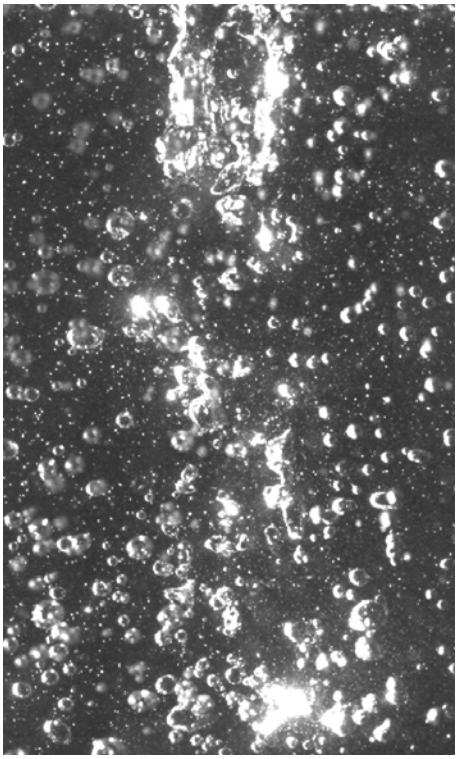

Fig. 2a Raw multiphase image

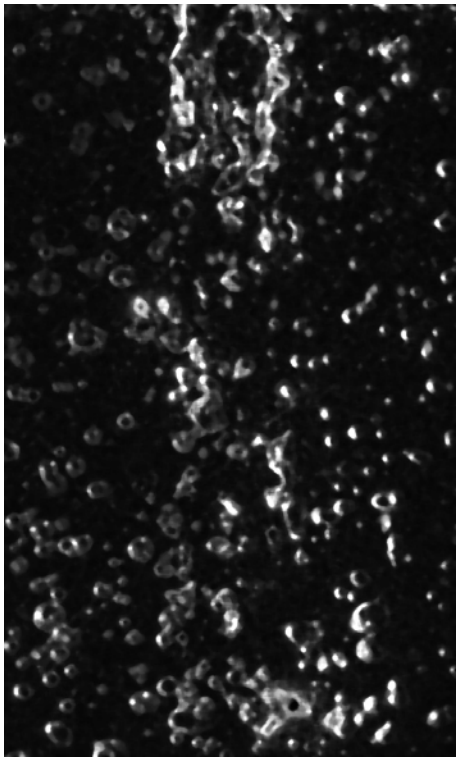

Fig. 2c Bubble-phase

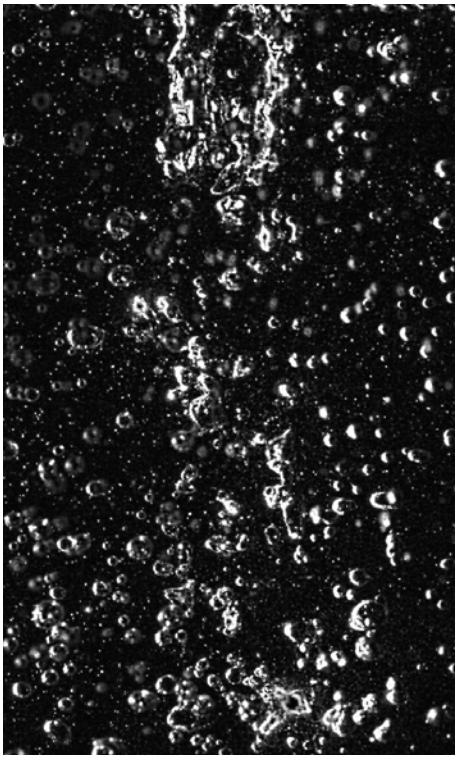

Fig. 2b Processed multiphase image

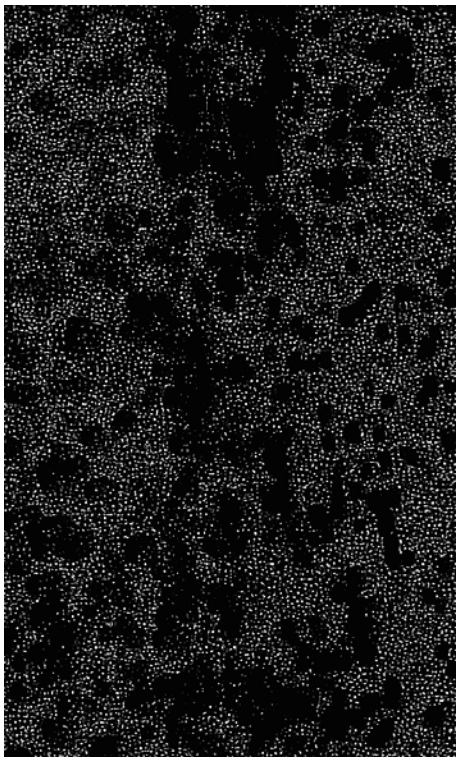

Fig. 2d Liquid-phase

The centerline axial velocities were found to be U_c = 1.2 and 1.9 m/s for *Re*=13,000 and 23,000, respectively. Both U_c values were used to normalize reported flow field data. Radial profiles of axial velocity component and U_c values for nozzle heights *H/d* = 0 and -1 were identical.

Figures 3 and 4 show the radial profiles of the normalized mean, u & v, and RMS, u' & v', velocities at an axial station located 0.25*d* downstream of the pipe nozzle for *Re* = 13,000 and 23,000, respectively.

All velocities are normalized by the centerline axial velocity at the pipe exit, U_c, while axial and radial distances are normalized by the pipe diameter, *d*. As expected, the radial components of the mean velocity, v, are close to zero within the jet, $|r/d| \le 0.5$, while the axial ones, u, display a power-law profile that is typical of fully developed pipe conditions. The radial profiles of the RMS velocities display distinct peaks at the edge of the jet. The lowest axial RMS component, $u' \approx 0.04$, was obtained at the jet center while the highest one, $u' \approx 0.15$, was obtained at $r/d = \pm 0.5$. Substantial differences between the radial and axial components of the RMS velocities confirm turbulence anisotropy.

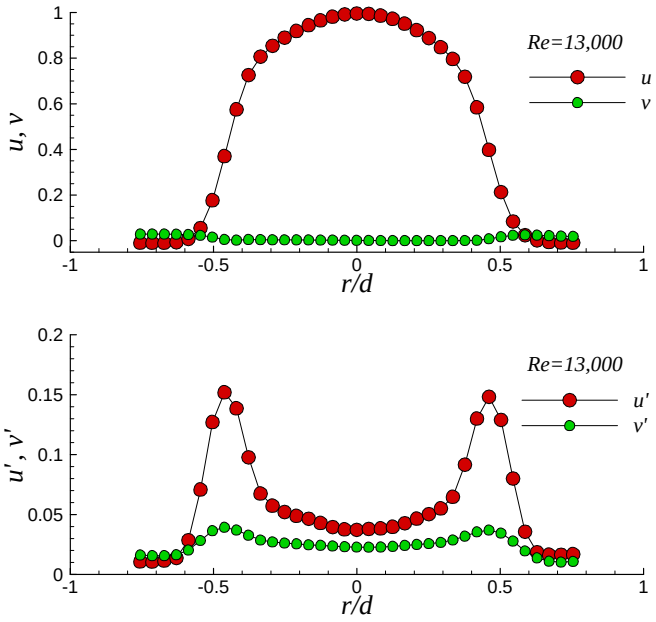

Fig. 3. Radial profiles of liquid-phase mean and RMS velocity components obtained 0.25d downstream the pipe nozzle for nozzle height of 0 at Reynolds number = 13,000

LIQUID-PHASE RESULTS

Mean velocity and turbulence characteristics of the liquid-phase in the flow-developing region are shown in Fig's 5, 6, 7, and 8. Fig's 5 and 6 correspond to *Re*=13,000 and represent the flow field in the absence of entrained air bubbles, *i.e.* single-phase impinging jet flow field. The *Re*=23,000 case, Fig's 7 and 8, represent the higher jet velocity case that resulted in air entrainment at jet impact. No air entrainment was observed for all studied Reynolds numbers when the nozzle was placed at the air-liquid interface, *i.e. H*=0.

Bubble entrainment suppresses liquid-phase mean velocities and enhances fluctuations in the streamwise direction, as shown in Fig's 7 and 8 for *Re*=23,000 and *H/d*=1 and 2. However, bubbles reduce radial RMS velocities of the liquid-phase and result in almost identical radial distributions within *z/d*=2-6, *H/d*=2 case shown in Fig. 8. The significant increase in the streamwise RMS velocities shown in Fig. 8 for *H/d*=2 is due to the substantially higher entrained bubbles population. Increasing the nozzle height to *H/d*=2 results in a global transition in the air entrainment and bubble generation mechanisms. This transition was visually observed and will be discussed in the next section, bubble-phase results. The streamwise RMS velocity values at the jet centerline, for *Re*=23,000 and nozzle height *H/d*=2, are u'=0.26, 0.177, 0.132 at *z/d*=2, 4 and 6, respectively.

Note that due to gravity, jet velocities at impact point, *i.e.* air-liquid interface, are expected to be higher than the initial ones out of the nozzle when *H*>0. For the simplified case of an initial centerline velocity at nozzle exit, U_c, accelerating under the influence of gravity only, the jet centerline velocity at impact point or interface, U_{ci}, can be estimated using:

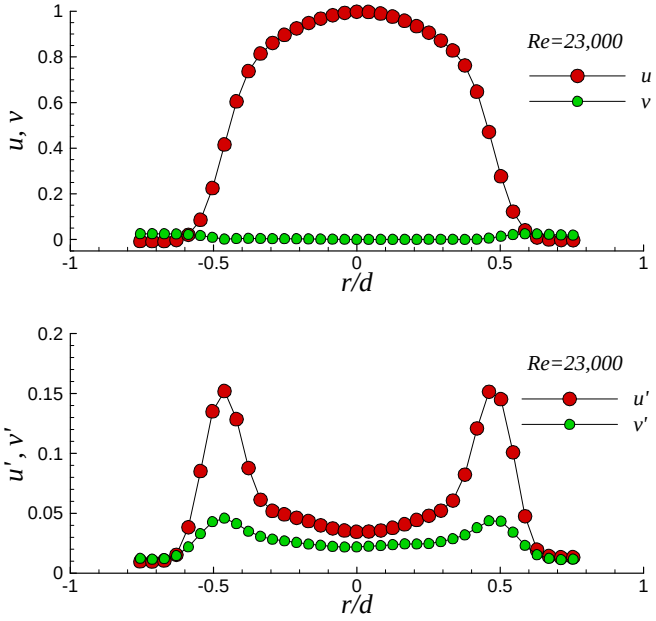

Fig. 4. Radial profiles of liquid-phase mean and RMS velocity components obtained 0.25d downstream the pipe nozzle for nozzle height of 0 at Reynolds number = 23,000

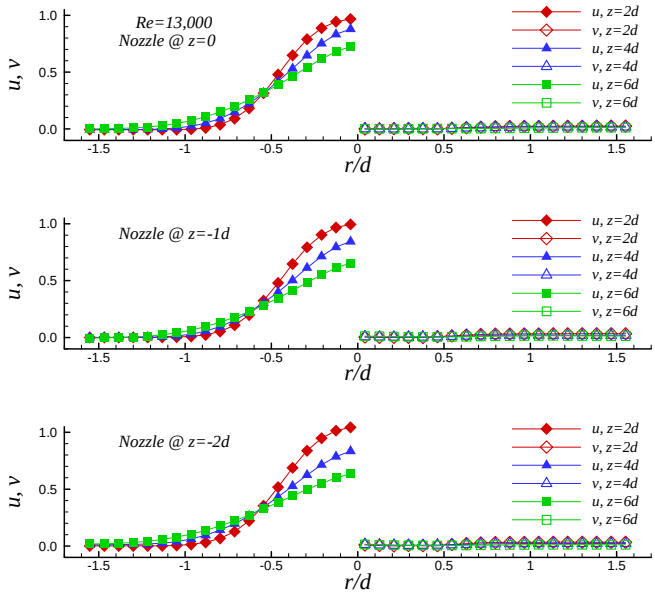

Fig. 5. Radial profiles of liquid-phase mean velocity components, *u and u*, obtained 2d, 4d and 6d beneath the impingement free surface for nozzle heights of 0, 1d and 2d at Reynolds number = 13,000

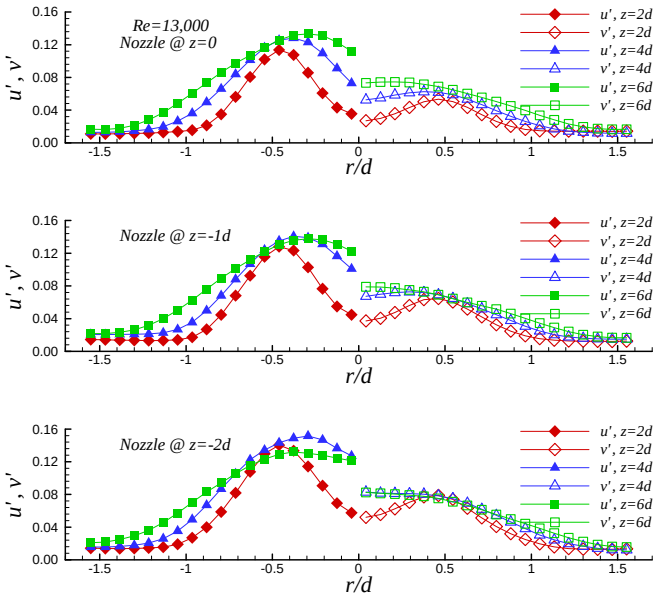

Fig. 6. Radial profiles of liquid-phase RMS velocity components, *u′ and u′*, obtained 2d, 4d and 6d beneath the impingement free surface for nozzle heights of 0, 1d and 2d at Reynolds number = 13,000

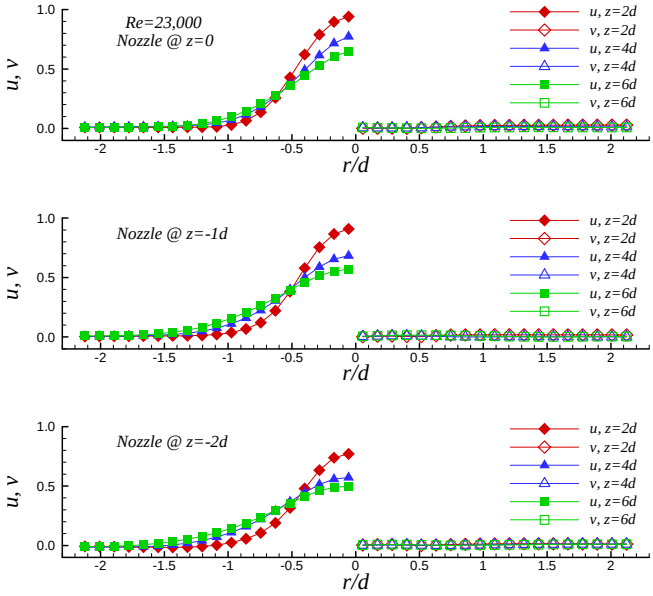

Fig. 7. Radial profiles of liquid-phase mean velocity components, *u and u*, obtained 2d, 4d and 6d beneath the impingement free surface for nozzle heights of 0, 1d and 2d at Reynolds number = 23,000

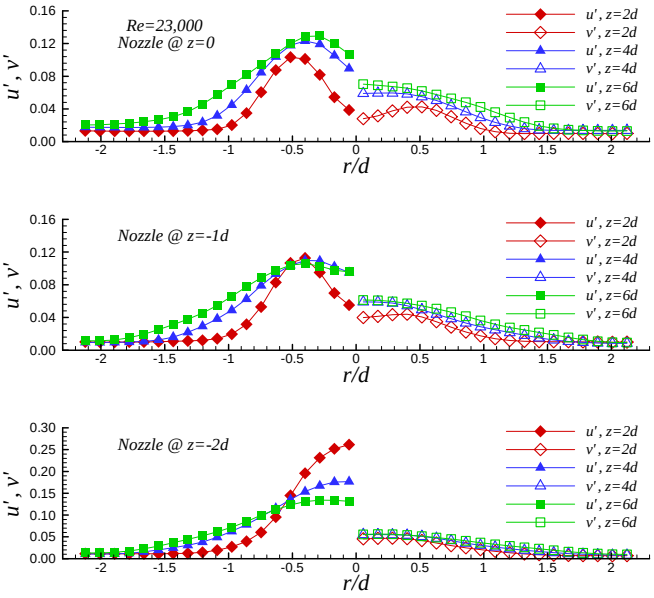

Fig. 8. Radial profiles of liquid-phase RMS velocity components, *u′ and u′*, obtained 2d, 4d and 6d beneath the impingement free surface for nozzle heights of 0, 1d and 2d at Reynolds number = 23,000

$$U_{ci} = \sqrt{U_c^{\,2} + 2gH} \qquad (1)$$

Using Eq. 1, the expected jet centerline velocity at impact point, taking into account change resulting from gravity driven acceleration only, is calculated and tabulated in Table 1 for all studied Reynolds numbers and nozzle heights.

The percentage increase in centerline velocities at impact point compared to those obtained at the nozzle exit for *Re*=13,000 is approximately twice that of *Re*=23,000.

	Re=13,000			*Re=23,000*		
H/d	U_c *(m/s)*	U_{ci} *(m/s)*	U_{ci}/U_c (%)	U_c *(m/s)*	U_{ci} *(m/s)*	U_{ci}/U_c (%)
1	1.2	1.29	107	1.9	1.96	103
2	1.2	1.37	114	1.9	2.01	106
3	1.2	1.44	120	1.9	2.06	109

Table 1 Jet centerline velocities at nozzle exit and at impact point for nozzle heights of 0, 1d and 2d and Reynolds number = 13,000 and 23,000

BUBBLE-PHASE RESULTS

Mean velocity and turbulence characteristics of the bubble-phase are shown in Fig's 9 and 10 for *Re*=23,000. Recall that there was no air bubbles entrainment in the *Re*=13,000 case.

For nozzle height *H/d*=1, individual air bubble entrainment was observed. Increasing the nozzle height to *H/d*=2 resulted in the development of an unstable air cavity along the impingement perimeter. The air cavity position fluctuated randomly, along the jet perimeter, with time. For nozzle heights of *H/d*=3 and higher, the air cavity seemed to form around most of the jet perimeter and extended to approximately *z/d*=2. Constant stretching and breakup of the cavity tip formed large air packets which were entrained below the air cavity, close to the annular jet shear layer. The entrained air packets broke up into smaller bubbles as they travelled further downstream.

Within the annular shear layer of the jet, $|r/d| \le 0.5$, the mean axial velocities, u, of the bubble-phase shown in Fig. 9, are substantially smaller than the liquid-phase ones shown in Fig. 7. However, further away from the jet core, $|r/d| \approx 2$, the flow field is dominated by the upward movement of the generated bubble population and the mean axial velocities, u, are higher than the ones obtained in the liquid-phase only case, *i.e. Re*=13,000 case shown in Fig. 7. The axial component of the mean velocity of bubbles, u, at $|r/d| \approx 2$ are tabulated in Table 2. They represent the bubble population rise and are shown to increase with nozzle height, *H*, reflecting larger bubble size creation.

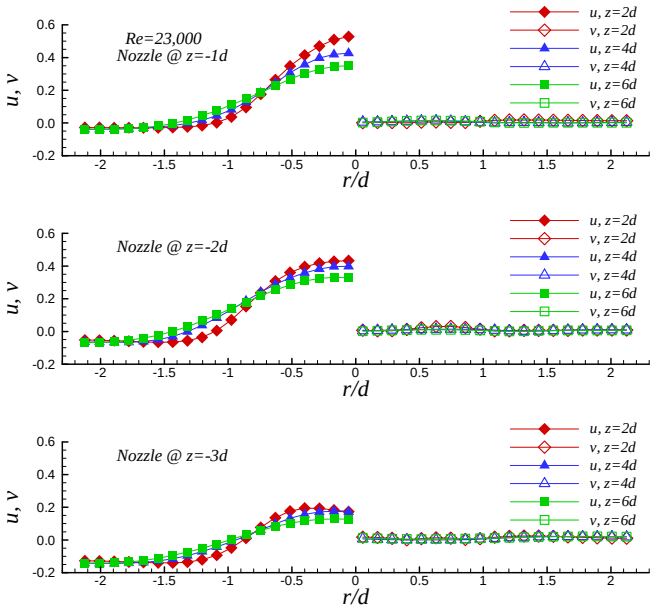

Fig. 9. Radial profiles of bubble-phase RMS velocity components, u *and* u, obtained 2d, 4d and 6d beneath the impingement free surface for nozzle heights of 0, 1d and 2d at Reynolds number = 13,000

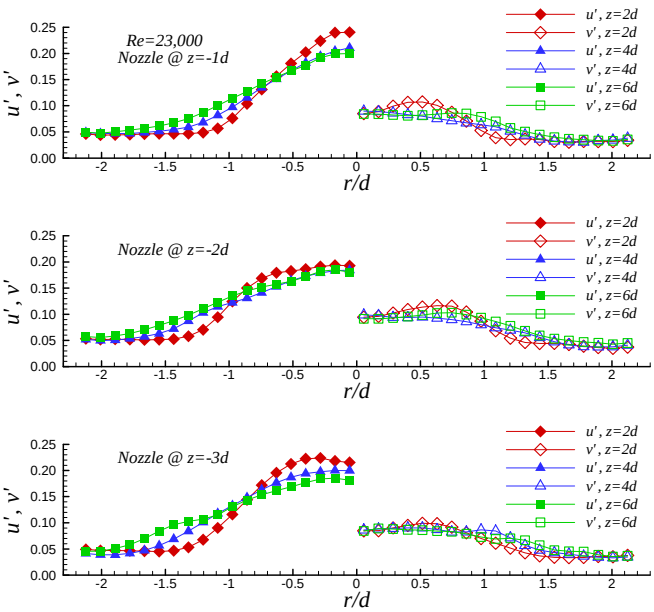

Fig. 10. Radial profiles of bubble-phase RMS velocity components, u' *and* u', obtained 2d, 4d and 6d beneath the impingement free surface for nozzle heights of 0, 1d and 2d at Reynolds number = 23,000

	Bubble rise velocity (m/s), from u at r/d=-2		
z/d	*H/d=1*	*H/d=2*	*H/d=3*
2	0.053	0.103	0.245
4	0.073	0.124	0.272
6	0.073	0.127	0.269

Table 2 Bubble rise velocity for nozzle heights of 1d, 2d and 3d at Reynolds number = 23,000

Measured turbulent intensities in the radial direction for the bubble-phase are substantially stronger than the corresponding intensities of the liquid-phase, as shown in Fig's 8 and 10.

CONCLUSIONS

An experimental study of a fully developed turbulent jet issuing from a long pipe and impinging normally a on a horizontal air-water interface has been conducted. PIV measurements were performed within the flow developing region for two Reynolds numbers, *Re*= 13,000, 23,000, and four nozzle-to-interface separation distances, *H/d*= -1, 0, 1, 2 and 3. In the case of *Re*= 13,000, a liquid-phase flow field was observed beneath the interface. However, increasing the Reynolds number to *Re*= 23,000 resulted in the formation of a bubbly two-phase flow field when the separation distance was one jet diameter or higher. Simultaneous PIV measurements of the liquid and bubble-phase velocities allowed for appropriate and detailed evaluation of the flow features of the weakly viscous system under consideration.

For nozzle height *H/d*=1, individual air bubble entrainment was observed. Increasing the nozzle height to *H/d*=2 resulted in the development of an unstable air cavity along the impingement perimeter. The air cavity position fluctuated randomly, along the jet perimeter, with time. For nozzle heights of *H/d*=3 and higher, the air cavity seemed to form around most of the jet perimeter and extended to approximately two jet diameters beneath the interface.

Strong modulation of liquid-phase turbulence due to the presence of bubbles results in higher turbulent intensities in the axial direction and lower ones in the radial direction. Bubble entrainment suppresses liquid-phase mean velocities and enhances fluctuations in the streamwise direction. Measured turbulent intensities in the radial direction for the bubble-phase are substantially stronger than those of the liquid-phase. The presence of bubbles reduces radial RMS velocities of the liquid-phase.

ACKNOWLEDGEMENTS

The author is grateful to Mr. Craig Goulbourne for helping with the experiment setup.

REFERENCES

[1] Chanson, H., Cummings, P., 1992, 'Aeration of the ocean due to plunging waves.' Research report, No. CE142, Department of Civil Engineering, University of Queensland, Australia.

[2] Lara, P., 1979, 'Onset of air entrainment for water jet impinging vertically on water surface,' Chem. Engng. Sci. **34**, pp. 1164–1165.

[3] Burgess, J.M., Molly, N.A., Mc Carthy, M.J., 1972. A note on plunging liquid jet reactor. Chem. Engng. Sci. **27**, pp. 442–445.

[4] Iciek, J., 1982, 'The hydrodynamics of a free liquid jet and their influence on direct contact heat transfer,' Int. J. Multiphase Flow **8** (3), pp. 239–249.

[5] Kusabiraki, D., Murota, M., Ohno, S., Yamagiwa, K., Yasuda, M., and Ohkawa, A., 1990, 'Gas entrainment rate and flow pattern in a plunging liquid jet aeration system using inclined nozzles,' J. Chem. Engng. Japan **23** (6), pp. 704–710.

[6] McKeogh, E.J., Ervine, D.A., 1981, 'Air entrainment rate and diffusion pattern of plunging liquid jets,' Chem. Engng. Sci. **36**, pp. 1161–1172.

[7] Lezzi, A.M., Prosperetti, A., 1991, 'The stability of an air film in a liquid flow,' J. Fluid Mech. **226**, pp. 319–347.

[8] Bin, A.K., 1993, 'Gas Entrainment by plunging liquid jets,' Chem. Eng. Sci, **48 (**21), pp. 3585-3630.

[9] Bonetto, F., Lahey, R.T., 1993, 'An experimental study on air carryunder due to a plunging liquid jet,' Int. J. Multiphase Flow **19** (2), pp. 281–294.

[10] Chanson, H., 1997. Air Bubble Entrainment in Free-surface Turbulent Shear Flows. Academic Press, London, UK, 401pp.

[11] Oguz, H.N., 1998, 'The role of surface disturbances in the entrainment of bubbles by a liquid jet,' J. Fluid Mech. **372**, pp. 189–212.

[12] Zhu, Y., Oguz, H.N., Prosperetti, A., 2000, 'On the mechanism of air entrainment by liquid jets at a free surface,' J. Fluid Mech. **404**, pp. 151–177.

[13] El Hammoumi, M., Achard, J.L., Davoust, L., 2002, 'Measurements of air entrainment by vertical plunging liquid jets,' Experiments in Fluids **32**, pp. 624–638.

[14] Davoust, L., Achard, J.L., El Hammoumi, M., 2002, 'Air entrainment by a plunging jet: the dynamical roughness concept and its estimation by a light absorption technique,' Int. J. Multiphase Flow **28**, pp.1541-1564.

[15] Chanson H, Manasseh R., 2003, 'Air entrainment processes in a circular plunging jet: void-fraction and acoustic measurements,' J Fluids Eng. **125**, 910-921.

[16] Iguchi, M., Okita, K. and Yamamoto, F., 1998, 'Mean velocity and turbulence characteristics of water flow in the bubble dispersion region induced by plunging water jet,' Int. J. Multiphase Flow 24 (4), pp. 523-537.

[17] Chanson H, Aoki S, Hoque A, 2004, 'Physical modelling and similitude of air bubble entrainment at vertical circular plunging jets,' Chem Eng Sci, **59** (4), pp. 747–58.

[18] Westergaard, Madsen, Marassi, and Tomasini, 2003, 'Accuracy of PIV Signals in Theory and Practice,' 5th International Symposium on Particle Image Velocimetry, Busan, Korea, September 22-24, Paper 3301.